https://doi.org/10.5194/egusphere-2026-5017
Preprint. Discussion started: 22 September 2026

Transcontinental transport of a massive SO_2 plume from the Tehran refinery explosion in March 2026 observed from space

Shangyi Liu[1,2], Cathy Clerbaux[2,3], Anne Boynard[2,4], Mingjian Gu[5], Chengli Qi[6], Bruno Franco[3], Lieven Clarisse[3], Shan Han[1], Mengya Sheng[1], Nicolas Theys[7], Zhao-Cheng Zeng[1,*]

[1] School of Earth and Space Sciences, Peking University, Beijing, China
[2] LATMOS/IPSL, Sorbonne Université, UVSQ, CNRS, Paris, France
[3] Université libre de Bruxelles (ULB), BLU-ULB research Center, Spectroscopy, Quantum Chemistry and Atmospheric Remote Sensing (SQUARES), Brussels, Belgium
[4] SPASCIA, Ramonville-Saint-Agne, Toulouse, France
[5] Shanghai Institute of Technical Physics, Chinese Academy of Sciences, Shanghai, China
[6] National Satellite Meteorological Center, China Meteorological Administration, Beijing, China
[7] Royal Belgian Institute for Space Aeronomy (BIRA-IASB), Brussels, Belgium

Correspondence to: Zhao-Cheng Zeng (zczeng@pku.edu.cn)

Abstract. Conflict-induced explosions can inject pollutants into the middle-to-upper troposphere, producing long-range transport with environmental impacts beyond the local scale. In March 2026, airstrikes on Tehran's refinery complex triggered massive explosions and fires, releasing sulfur dioxide (SO_2) and carbonaceous aerosols. This study utilizes the data from a hyperspectral infrared satellite constellation (CrIS, IASI, and HIRAS) to track the explosion-related SO_2 plume with high frequency. The plume was first detected by CrIS at 22:01 UTC on 7 March at approximately 8.2 km altitude. Retrievals yield a peak SO_2 mass of approximately 3 kt, equivalent to the emissions of a minor volcanic eruption. Satellite observations capture the plume's transcontinental transport over roughly four days, demonstrating good agreement with HYSPLIT forward trajectories simulations. Comparison with CAMS SO_2 forecasts reveal that the model reproduces the transport of regional anthropogenic SO_2 but fails to capture the explosion plume. This study highlights the importance of satellite observations in monitoring emissions from conflict-induced extreme events and accurately assessing their long-range environmental impacts. The Tehran event also provides new insights into the potential global atmospheric impacts from a wider conflict.

Keywords: Tehran refinery explosion, sulfur dioxide (SO_2), satellite remote sensing, transcontinental transport, conflict-induced emissions

https://doi.org/10.5194/egusphere-2026-5017
Preprint. Discussion started: 22 September 2026

1 Introduction

Modern armed conflicts increasingly target energy and industrial infrastructure. Historical events such as the 1991 Kuwait oil-well fires **(Hobbs and Radke, 1992)**, the 2016 Al-Mishraq sulfur plant fire in Iraq **(Björnham et al., 2017)**, and and attacks on industrial facilities during the Russia–Ukraine war **(Rawtani et al., 2022)** all released massive toxic pollutants and triggered regional air quality crises. Beyond regional impacts, intense explosions or sustained fires can generate pyro-convective updrafts, injecting pollutants like sulfur dioxide (SO_2) from the planetary boundary layer into the free troposphere **(Fromm et al., 2010)**. There, pollutants chemical lifetime is extended **(Long et al., 2017)** and entrainment into mid-latitude westerly jets enable transport far beyond the regional scale, which is less focused in previous studies.

During the nighttime of March 7–8, 2026, Israeli airstrikes on oil refineries and fuel depots in Tehran triggered massive explosions and fires **(Al Jazeera, 2026; BBC, 2026)**. The combustion of sulfur-rich crude oil injected large amounts of SO_2 and carbonaceous aerosols into the atmosphere, causing severe acute hazards such as "black rain" across the Tehran metropolitan area **(CEOBS, 2026; Khaleej Times, 2026)**. Compared to other co-emitted pollutants, SO_2 exhibits a suitable lifetime (several days) and distinct spectral features, making it an ideal tracer for tracking conflict-induced transcontinental transport.

Crucially, such explosive anthropogenic emissions represent a critical blind spot in operational air quality forecast models. Systems like the Copernicus Atmosphere Monitoring Service (CAMS) rely heavily on static emission inventories for anthropogenic sources and restrict their SO_2 data assimilation primarily to strong volcanic plumes (e.g., TROPOMI SO2 > 5 DU near known volcanoes) **(Flemming et al., 2015; Inness et al., 2019)**. Consequently, CAMS systematically failed to capture the unpredictable, massive plumes generated by the Tehran explosions.

With operational models hindered by these limitations, satellite remote sensing becomes the only viable approach to characterize such events. SO_2 can be globally tracked using sensors operating in both the ultraviolet (UV) (e.g., OMI, OMPS, TROPOMI) **(Krotkov et al., 2006; Yang et al., 2013; Theys et al., 2017)** and thermal infrared (IR) (e.g., IASI, CrIS, HIRAS, GIIRS) **(Clarisse et al., 2011; Bauduin et al., 2016; Hyman and Pavolonis, 2020; Zeng et al., 2025; Liu et al., 2026)** spectral ranges. A recent study attempted to assess this event using UV satellite observations **(Yin et al., 2026)**. However, UV-based retrievals intrinsically lack explicit physical constraints on the plume altitude. By assuming the plume was confined solely to the lower troposphere, such methods severely overestimate both the SO_2 column densities and the total emitted mass. Furthermore, their analysis focused exclusively on the initial regional dispersion, failing to capture the plume's subsequent transcontinental transport and thereby severely underestimating its spatial impact.

To overcome these critical blind spots, we deploy a synergistic hyperspectral IR satellite constellation to accurately retrieve the SO_2 layer height and column density, and to track its full transcontinental life cycle. Compared to UV sensors, IR sensors offer unique advantages, including day-and-night operational capabilities, the ability to detect SO_2 plume heights, and significantly lower retrieval noise for low-concentration plumes in the mid-to-upper troposphere. In this study, our constellation consists of CrIS (afternoon orbit), IASI (mid-morning orbit), and FY-3E/HIRAS (dawn-dusk orbit), enabling six

https://doi.org/10.5194/egusphere-2026-5017
Preprint. Discussion started: 22 September 2026

dense overpasses per day over Tehran (Fig. 1c). These observations are processed using a Hyperspectral Range Index (HRI) based retrieval algorithm to estimate SO_2 total columns and layer heights. For comprehensive spatiotemporal analysis, we complement the MODIS Fire Radiative Power (FRP) product to track the explosion and sustained combustion, and the NOAA HYSPLIT forward trajectory model to simulate the SO_2 plume transmission pathways. TROPOMI observations and the EDGAR v8.1 inventory are jointly utilized to isolate the explosion signal from the regional anthropogenic background. Furthermore, CAMS global atmospheric composition forecasts were utilized to help identify anthropogenic emissions, analyze its transport pathways, and cross-compare with the satellite observations.

https://doi.org/10.5194/egusphere-2026-5017
Preprint. Discussion started: 22 September 2026

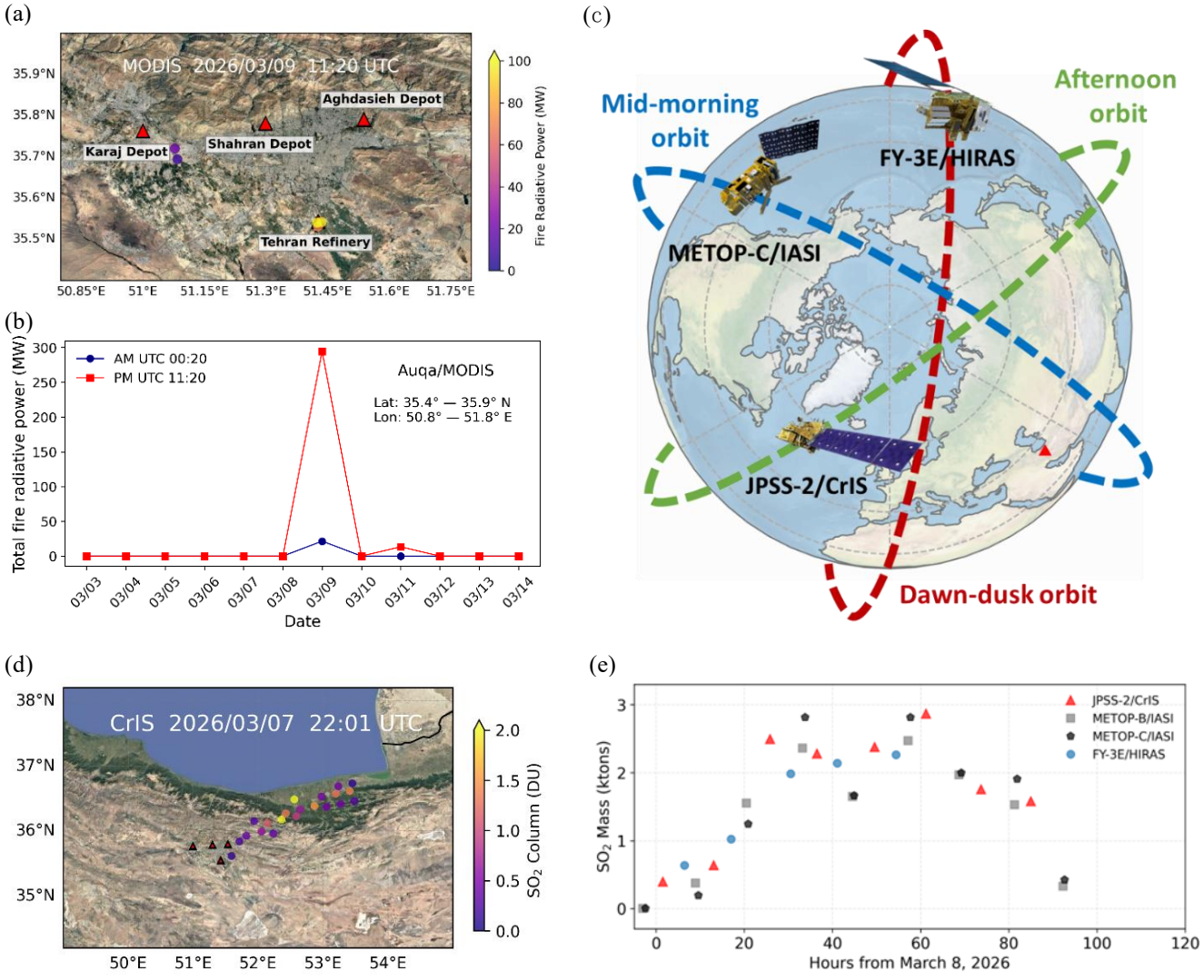

Figure 1: (a) Spatial distribution of Fire Radiative Power (FRP) derived from MODIS at 11:20 UTC on March 9, 2026. Red triangles denote the locations of the attacked refineries and oil depots. (Source: Al Jazeera, https://www.aljazeera.com/features/2026/3/9/israeli-attacks-on-iran-fuel-sites-aim-to-break-resilience-of, last accessed: 4 June 2026). (b) Time series of the total MODIS FRP over the region shown in panel (a) during the 12-day period surrounding the explosion. (c) Schematic of the hyperspectral infrared satellite constellation employed (comprising mid-morning, afternoon, and dawn-dusk orbits), with the red triangle marking the location of Tehran. (d) The first SO_2 total column (DU) result detected by the satellite constellation after the explosion, captured by CrIS at 22:01 UTC on March 7, 2026. The four red triangles correspond to the facility locations marked in panel (b). (e) Time series of total SO_2 mass (ktons) derived from the satellite constellation (CrIS, IASI, and HIRAS) following the attack, from March 8 to 11, 2026. Satellite imagery in panels (a) and (d) is provided by Google Maps. Administrative boundaries across all maps and the globe basemap in panel (c) are sourced from Natural Earth.

https://doi.org/10.5194/egusphere-2026-5017
Preprint. Discussion started: 22 September 2026

2 Results and discussion

2.1 Satellite-retrieved SO_2 column evolution and HYSPLIT trajectory simulations

Figure 1a displays the spatial distribution of the attacked refineries and oil depots in Tehran alongside the MODIS FRP results at 11:20 UTC on March 9 (approximately 1.5 days after the explosion). The high FRP values coincide closely with the facility locations, confirming the sustained combustion following the attack. Fig. 1b illustrates the mean FRP time series over this domain from March 3 to 14, showing that MODIS only detects obvious FRP signals on March 9. The absence of FRP signal following the explosion on March 8 is attributed to the extensive cloud cover over the region (from NASA worldview at https://worldview.earthdata.nasa.gov/, not shown). Fig. 1d shows the first satellite observation of the SO_2 plume after the explosion, acquired by CrIS at 22:01 UTC on 7 March. For this initial detection, the retrieved maximum SO_2 total column is approximately 2.2 DU, with a mean plume height of 8.2 km.

The spatial distributions of the estimated SO_2 layer heights are presented in Figs. S1 and S2, where the red boxes delineate the plume domains primarily produced by the explosion. Other regional SO_2 enhancements are likely attributed to different anthropogenic emissions (detailed in Section 3.2). Fig. S3 displays the temporal evolution of the mean estimated SO_2 layer height and standard deviation. The retrieved mean altitude initiated at 8.2 km and gradually ascended, distributing within the 11 to 15 km range, which corresponds approximately to the upper troposphere and tropopause in the mid latitude. Both CrIS and IASI layer height estimates exhibit large standard deviations, particularly during the latter part of the study period. This is likely attributable to the relatively low SO_2 column densities (mostly < 0.5 DU) and the resulting large retrieval uncertainties in layer height estimates. Nevertheless, their error ranges and mean values overlap to a certain extent. The height discrepancy between the two platforms may stem from the higher spectral resolution of IASI, which enables deeper atmospheric sounding because absorption lines are more clearly resolved. The HIRAS SO_2 layer heights are not displayed because the higher spectral noise of the instrument leads to large uncertainties in the retrievals. Consequently, the median height derived from the temporally nearest IASI observation is directly utilized for the HIRAS physical retrieval.

The retrieved SO_2 total columns are shown in Figs. 2 and S4. The columns estimated by the three satellites exhibit reasonable consistency. IASI retrievals appear visually cleaner than those from CrIS and HIRAS, likely because the operational IASI product applies stricter filtering criteria than the algorithm used in this study. Furthermore, the TROPOMI SO_2 products are introduced for qualitative comparison with the infrared satellite retrievals. As shown in Fig. S5, TROPOMI and CrIS SO_2 columns exhibit good spatial agreement. However, quantitative comparisons remain challenging. The operational TROPOMI DOAS product provides retrievals at multiple assumed heights (1, 3, 7, and 15 km), but the retrievals over clouds have large uncertainty.

To quantify the emission, SO_2 total columns within the explosion plume (red boxes in Figs. S1 and S2) are re-gridded to 0.5° resolution and integrated. As shown in Fig. 1e, the SO_2 mass estimates show good consistency across sensors. The total SO_2 mass peaks at approximately 3 kt on the morning of 9 March, as retrieved from IASI, which is equivalent to only a few one-tenth of the SO_2 released by a typical small-to-moderate volcanic eruption **(Carn et al., 2016)**. Our estimate is an order

https://doi.org/10.5194/egusphere-2026-5017
Preprint. Discussion started: 22 September 2026

of magnitude lower than the ~30 kt reported by a recent UV study **(Yin et al., 2026)**, which severely overestimated the mass due to an erroneous lower-tropospheric assumption without explicit altitude retrieval. For comparison, IASI observations of the 2016 Al-Mishraq plume derived a mass peak exceeding 30 kt. Noted that despite its small magnitude, the plume remains detectable in the upper troposphere for about 4 days (several times longer than the typical boundary-layer SO_2 lifetime of approximately one day, **Long et al., 2017**). This underscores the critical role of injection height in extending the atmospheric lifetime of pollutants and enabling long-range transport **(Carn et al., 2016)**. Additionally, the mass estimates from the two IASI instruments show some differences, which can be attributed primarily to differences in the retrieved layer heights (cf. Fig. S3).

Furthermore, the NOAA HYSPLIT trajectory model is utilized to simulate the forward transport of the explosion plume and compare it with satellite observations. The model is driven by the Global Data Assimilation System (GDAS1) meteorological dataset with a 1° spatial resolution and a 3-hour temporal resolution. We conduct a 100-hour forward simulation using the ensemble model. The simulation is initialized using the mean latitude, longitude, observation time, and plume heights (tested at 8 and 9 km) derived from the first satellite observation of the SO_2 plume (Fig. 1e). The model runs incorporate two different vertical motion calculation methods: isentropic and model vertical velocity. As shown in Figure S6, results demonstrate that the simulated horizontal transport pathways from all four configurations match the spatial distribution of the satellite observations well. However, the simulated vertical evolution of the plume is inconsistent with the satellite-retrieved layer heights. This discrepancy is likely attributable to the self-lofting effect driven by the radiative heating of co-emitted black carbon aerosols from the oil fires **(Yu et al., 2019)**, which is not parameterized in the HYSPLIT vertical motion calculations.

2.2 Comparison with CAMS forecasts and source attribution

Figure S10 presents the spatial distribution of CAMS 500 hPa SO_2 forecasts at 00:00 and 12:00 UTC daily from 7 to 11 March. Starting on March 7, a distinct SO_2 enhancement appears near the Iraq and Turkey region, followed by rapidly eastward and northward transport with gradual dilution. Fig. S11 compares the CAMS simulations with CrIS retrievals, noting the time differences between model outputs and satellite overpasses. The results demonstrate that the satellite observations capture the transport and dispersion of this SO_2 plume, matching the CAMS simulations well. CrIS also continued to capture the plume after it had been diluted (e.g., on 10 March), whereas these weaker signals are largely absent in the IASI product, likely filtered out during post-processing (Figs. 2 and S4). However, while the CAMS model successfully simulates the transport of this plume, it completely missed the SO_2 emitted from the Tehran explosion. This omission occurs because CAMS represents anthropogenic sources using static emission inventories and restricts its dynamic SO2 data assimilation exclusively to volcanic plumes, rendering it inherently blind to sudden anthropogenic explosions.

We further investigated the background SO_2 plume originating near the Iraq-Turkey border to isolate it from the explosion signal. Fig. S7 presents the TROPOMI tropospheric NO_2 columns and SO_2 slant columns from March 6 to 11. The results reveal persistent high NO_2 values across the region, indicating the presence of anthropogenic pollution, particularly in Iraq. Previous studies have also reported point source emissions of NO_2 and SO_2 in this region **(Fioletov et al., 2020; Beirle et al.,**

https://doi.org/10.5194/egusphere-2026-5017
Preprint. Discussion started: 22 September 2026

2021). The SO_2 observations suggest that the plume source may be located near the border region of Turkey, Iraq, and Iran, or may originate from surrounding countries and be transported into this border area (as seen on 7 and 8 March). This is also supported by the EDGAR inventory for 2022 (the most recent year available) in Fig. S8, which confirms dense SO_2 emissions in this region caused by refineries, energy transformation, and industrial processes. Fig. S9 presents the CAMS SO_2 total column results from March 6 to 11 at 12:00 UTC. The figure similarly displays persistent high SO_2 values in this region, with the high-value center moving to the Iraq-Turkey border region on March 7 and initiating a northeastward transport on March 8. Combining these results, we hypothesize that this SO_2 plume is attributed to anthropogenic emissions from the countries in this region, which entered the free troposphere under local meteorological influences and subsequently underwent long-range transport.

Additionally, as the explosion plume continued eastward and reached eastern China, the total SO_2 mass time series exhibits an unexpected secondary peak around March 10 (Fig. 1e). This mass enhancement is likely attributed to the explosion plume mixed with the anthropogenic SO_2 emissions over Eastern China and Japan, making them difficult to separate in the mass calculation. Fig. S12 compares IASI SO_2 total columns with the CAMS 500 hPa SO_2 forecasts from 9 to 11 March. The IASI observations capture the SO_2 enhancement over eastern China (potentially local pollution) and its drift toward Japan. On 10 March, this plume spatially overlaps with the explosion plume. The CAMS simulations similarly reveal an SO_2 enhancement in the free troposphere over this region during this period.

3 Conclusions and outlook

Using a multi-orbit hyperspectral IR constellation, we tracked the March 2026 Tehran refinery explosions, observing approximately 3 kt of SO_2 injected into the upper troposphere and undergoing transcontinental transport within four days. Since most anthropogenic pollutants remain confined within the boundary layer, previous studies have primarily focused on massive emission events and their significant regional impacts. However, our findings demonstrate that even small-scale sudden emissions can achieve long-range transport when driven by intense pyro-convection. This study highlights the critical role of high-frequency hyperspectral satellites in overcoming the limitations of current forecast models, quantifying conflict-induced emissions, and assessing their environmental effects.

By extension, the Tehran event serves as a critical proxy for the atmospheric consequences of large-scale conflicts. Systematic destruction of energy infrastructure could inject unprecedented quantities of aerosols and SO_2 directly into the stratosphere, triggering severe climate feedbacks such as surface cooling, disrupted precipitation, and accelerated ozone depletion **(Bakan et al., 1991; Rawtani et al., 2022; Solomon et al., 2022)**. Therefore, utilizing high-frequency satellite observations to identify and continuously monitor these extreme emissions is not only a scientific necessity for assessing global climate risks, but also a crucial step toward formally integrating war-induced environmental damage into the global climate governance framework **(Lawrence et al., 2015)**.

https://doi.org/10.5194/egusphere-2026-5017
Preprint. Discussion started: 22 September 2026

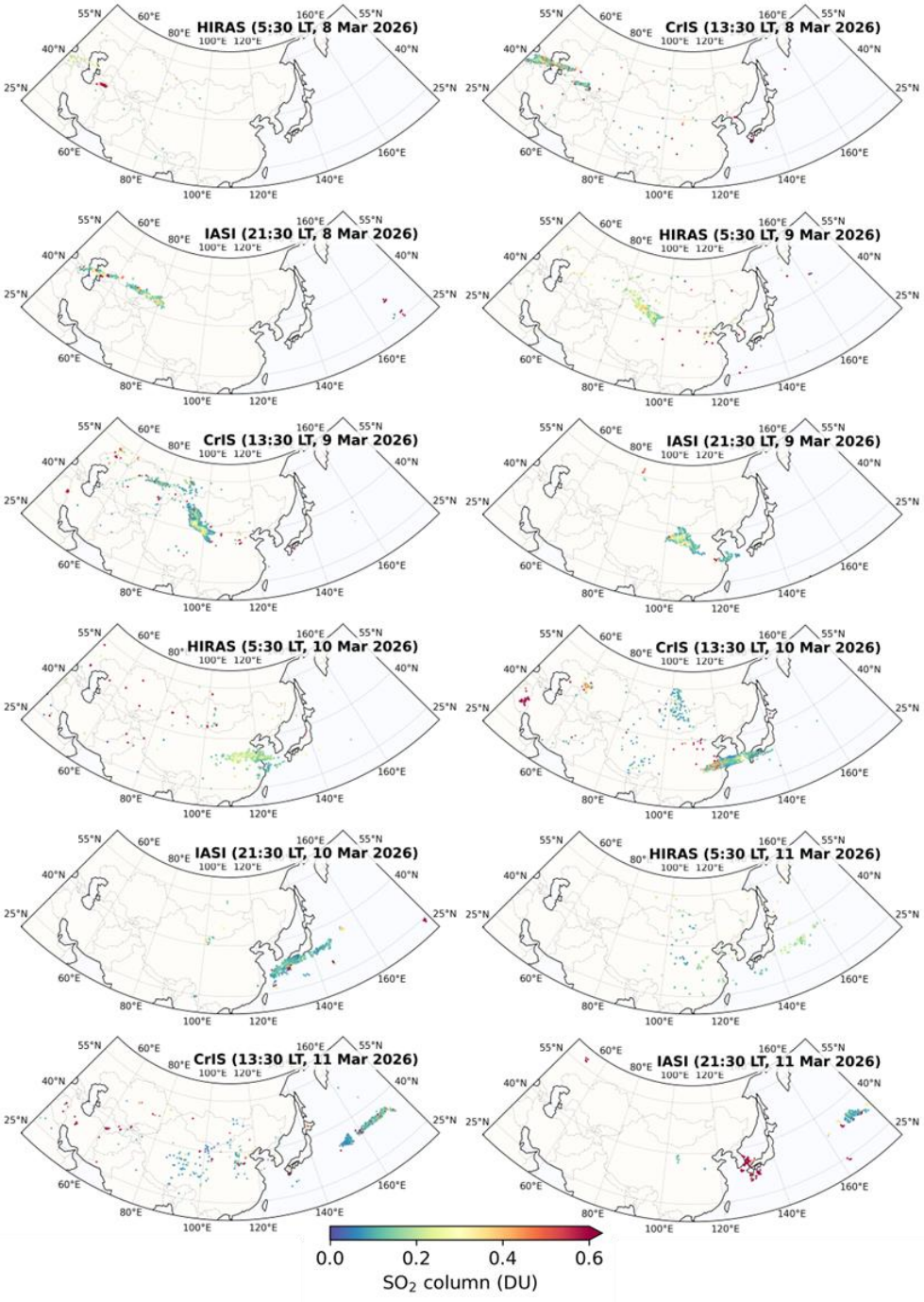

Figure 2: Spatiotemporal evolution of SO_2 total columns retrieved from the satellite constellation from March 8 to 11, 2026. For clarity, one overpass per satellite per day is shown, corresponding to local times (LT) of approximately 05:30 (HIRAS), 13:30 (CrIS), and 21:30 (Metop-C/IASI). The remaining overpasses are provided in Figure S4.

https://doi.org/10.5194/egusphere-2026-5017
Preprint. Discussion started: 22 September 2026

Appendix A: Data and processing

The SO_2 plume is tracked using hyperspectral IR sounders across three orbits: JPSS-2/CrIS (~01:30 AM/PM local time), Metop-B/C IASI (~08:30 and ~09:30 AM/PM), and FY-3E/HIRAS-II (~05:30 AM/PM), shown in Fig.1c. For CrIS and HIRAS, an HRI-based full-physical retrieval algorithm processes Level-1B radiances within the 1208–1400 cm^{-1} spectral range (SO_2 v3 band). This algorithm integrates HRI detection **(Walker et al., 2011)**, whitening transformation **(De Longueville et al., 2021; Manolakis et al., 2016)**, and the Optimal Estimation Method **(Rodgers, 2000)** to retrieve layer heights and total column densities (detailed in the Appendices B, C and D). For IASI, the v4.5 Level-2 products are used **(Clarisse et al., 2026)**. To support our analysis, MODIS Fire Radiative Power (FRP) data (MYD14 and MOD14) **(Giglio et al., 2016)** track the sustained combustion of the attacked facilities. Plume transmission pathways are simulated using the NOAA HYSPLIT forward trajectory model **(Stein et al., 2015)**. Background anthropogenic emissions are distinguished from the explosion signal using TROPOMI SO_2 **(Theys et al., 2017)** and NO_2 **(van Geffen et al., 2022)** products alongside the EDGAR v8.1 inventory **(Crippa et al., 2024)**. Finally, CAMS atmospheric composition forecasts are employed to help identify anthropogenic emissions, trace transport pathways and cross-compare with satellite observations **(Flemming et al., 2015; Inness et al., 2019)**.

Appendix B: The forward model

The forward radiative transfer simulations in this study are driven by the FengYun Low Earth Orbit Atmospheric Infrared Retrieval (FY-LeoAIR) framework **(Zeng, 2025)**. The top-of-atmosphere radiance received by the sensor is mathematically modeled as the summation of four distinct radiative components: surface thermal emission, upwelling atmospheric emission, downwelling atmospheric radiance reflected by the surface, and reflected incoming solar radiation **(Zeng et al., 2023)**. Molecular and aerosol scattering are considered negligible in the targeted thermal infrared window (1208–1400 cm^{-1}) and are therefore excluded to optimize computational efficiency. For numerical implementation, the atmosphere is discretized into a 34-layer pressure grid ranging from the 1000 hPa up to 1 hPa, spaced at intervals of approximately 1 km below 25 km and increasing to 2.5 km above this altitude.

Input parameters for the forward model are derived from multiple high-resolution datasets. Profiles for atmospheric temperature, water vapor, and ozone, along with surface skin temperature and pressure, are sourced from the European Centre for Medium-Range Weather Forecasts (ECMWF) ERA5 reanalysis **(Hersbach et al., 2020)**. The CO_2 profiles are obtained from the CAMS global atmospheric composition forecasts. The a priori vertical distributions of other interfering species (CH_4, N_2O and HNO_3) are initialized using the Line-By-Line Radiative Transfer Model (LBLRTM, v12.11) standard atmospheric backgrounds **(Atmospheric and Environmental Research, 2025)**. Surface emissivity is derived from the UW-Madison Global Infrared Land Surface Emissivity database **(Seemann et al., 2008)**, while the ocean surface emissivity is calculated adopting the model in **Masuda et al. (1998)**. To speed up the calculations, gas absorption coefficients are pre-computed using LBLRTM to construct look-up tables (LUTs) across various temperature and pressure levels.

The forward radiative transfer model is employed to calculate the SO_2 Jacobian vectors, which are subsequently utilized in the retrieval algorithm (Appendix C) to determine the SO_2 layer height and total column. These Jacobians are

https://doi.org/10.5194/egusphere-2026-5017
Preprint. Discussion started: 22 September 2026

derived through finite difference calculations using a total SO_2 column of 1 Dobson Unit (DU), representing approximately ten times the a priori value. Furthermore, to generate the altitude-dependent Jacobians required for the layer height estimation, a partial SO_2 column of 10 DU is sequentially assigned to individual layers at varying atmospheric altitudes to simulate the spectral response across different heights.

Appendix C: Full-physical retrieval of SO_2

In this study, a full-physical retrieval algorithm based on the framework of **Carboni et al. (2012)** and **Zeng et al. (2025)** is utilized to process CrIS and HIRAS Level-1B spectra within the 1208–1400 cm^{-1} spectral range (covering the SO_2 $\nu 3$ absorption band). The algorithm integrates HRI detection, whitening transformation, and OEM to identify SO_2-enhanced pixels and retrieve layer height and total column density. The forward radiative transfer model used to simulate theoretical spectra is described in Appendix B.

The HRI quantifies the spectral interval containing the target gas's sensitive channels into a single value representing its spectral contribution. It is defined as:

$$\boldsymbol{HRI} = \frac{\boldsymbol{K^T S^{-1}(y-\bar{y})}}{\sqrt{\boldsymbol{K^T S^{-1} K}}}, \quad (1)$$

where $\boldsymbol{K}$ is the SO_2 Jacobian vector, and $\bar{\boldsymbol{y}}$ and $\boldsymbol{S}$ are the mean background spectrum and associated covariance matrix, respectively. In this work, $\bar{\boldsymbol{y}}$ and $\boldsymbol{S}$ are constructed from all CrIS and HIRAS observations acquired on March 6, 2026 (one day before the explosion) over the potential plume transport region (30°W to 180°E, 25°N to 55°N). The Jacobian $\boldsymbol{K}$ is calculated using the approach in **Zeng et al. (2025)**. In our detection scheme, pixels exhibiting an HRI value greater than 3 (corresponding to a 99% confidence level) are initially flagged as potential SO_2 enhancements. A lower threshold of 2 was also evaluated. It produced a similar spatial extent for the SO_2 plume but resulted in noisier background. However, HRI is sensitive but prone to false detection when spectral interferences (e.g., water vapor, other trace gases, or anomalous surface emissivity) overlap with the SO_2 absorption band **(Clarisse et al., 2013)**. Therefore, whitening transformation is applied to assess whether elevated HRI values genuinely originate from SO_2 enhancement. It removes background signal and highlights the target gas absorption features. A detailed description is provided in Appendix D. As shown in Fig. A1, an example of a whitened CrIS spectrum sampled within the detected plume exhibits a good match with the whitened Jacobian, which confirms a true SO_2 signal.

The spectra screened by this whitening transformation are subsequently used for HRI-based layer height estimation. The Jacobian in Eq. (1) is replaced by altitude-dependent Jacobians pre-calculated at 1 km intervals. The retrieved layer height corresponds to the altitude yielding the maximum HRI value, as the observed spectrum best matches the theoretical SO_2 spectral feature at this specific altitude **(Clarisse et al., 2014)**.

Finally, the SO_2 total columns are quantified based on the OEM framework. The algorithm does not explicitly derive other geophysical parameters such as water vapor and clouds. Instead, these unknown interferences are treated as generalized error sources and encapsulated within a comprehensive measurement error covariance matrix $\boldsymbol{S_\varepsilon}$. This matrix is constructed

https://doi.org/10.5194/egusphere-2026-5017
Preprint. Discussion started: 22 September 2026

by statistically characterizing the residuals between observed and simulated spectra in SO_2-free scenarios. The optimal estimate is obtained by minimizing the following cost function:

$$\boldsymbol{J(x)} = [\boldsymbol{y} - \boldsymbol{F(x,b)}]^T \boldsymbol{S_\varepsilon^{-1}} [\boldsymbol{y} - \boldsymbol{F(x,b)}] + (\boldsymbol{x} - \boldsymbol{x_a})^T \boldsymbol{S_a^{-1}} (\boldsymbol{x} - \boldsymbol{x_a}), \quad (2)$$

where $\boldsymbol{y}$ represents the observed spectrum, the state vector $\boldsymbol{x}$ includes only the SO_2 total column and surface temperature, $\boldsymbol{F}$ is the forward model simulation, $\boldsymbol{x_a}$ is the a priori state vector, and $\boldsymbol{S_a}$ is the a priori covariance matrix. Weak a priori constraints are applied (500% uncertainty for SO_2 column, 20 K for surface temperature). The simulated spectra are generated using ERA5 reanalysis data (e.g., water vapor and temperature) from March 6, 2026, over the potential pollution region, with the zero SO_2 concentration fixed.

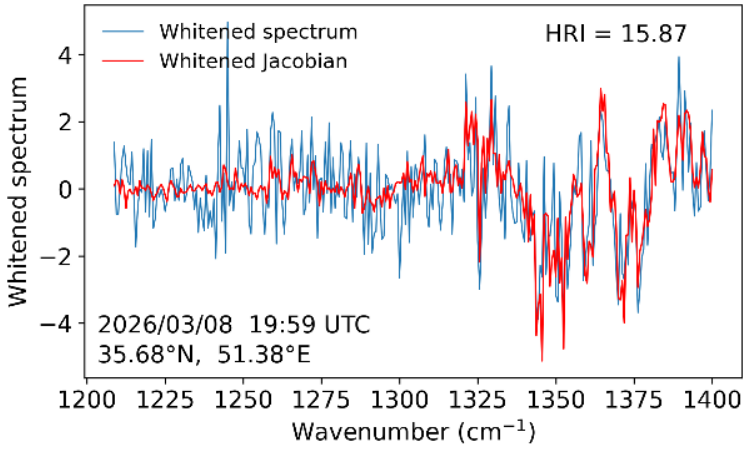

Figure A1: An example of the whitened spectrum (blue) and whitened SO_2 Jacobian (red) from a CrIS observation within the SO_2 plume.

Appendix D: Whitening transformation

To robustly verify whether an anomalous spectral contribution detected by the HRI genuinely originates from SO_2, a complementary spectral whitening transformation is applied **(De Longueville et al., 2021)**. This technique transforms the originally observed spectrum $\boldsymbol{y}$ into a whitened spectrum $\boldsymbol{y_{whitened}}$ by utilizing the inverse square root of the background covariance matrix ($\boldsymbol{S}$):

$$\boldsymbol{y_{whitened}} = \boldsymbol{S^{-\frac{1}{2}}}(\boldsymbol{y} - \bar{\boldsymbol{y}}). \quad (3)$$

This equation effectively removes the majority of the background signal by subtracting the mean background spectrum ($\bar{\boldsymbol{y}}$) and assigning the statistical variability of the background as a weight. Through this mathematical transformation, the spectrum of each channel is converted into uncorrelated random variables possessing an ideal zero mean and a unit standard deviation. Because this operation converts generalized background noise into pure white noise, it is referred to as "whitening" **(Manolakis et al., 2016)**. Similarly, the target gas Jacobian $\boldsymbol{K_{whitened}}$ can also be whitened using the same background clutter matrix:

$$\boldsymbol{K_{whitened}} = \boldsymbol{S^{-\frac{1}{2}}K}. \quad (4)$$

https://doi.org/10.5194/egusphere-2026-5017
Preprint. Discussion started: 22 September 2026

When a spectrum is whitened, any channel exhibiting an anomaly that deviates from the mean by more than one standard deviation is highly suspected to contain contributions from an external absorber. By visually or quantitatively comparing the whitened spectrum ($\boldsymbol{y_{whitened}}$) with the appropriately scaled whitened Jacobian ($\boldsymbol{K_{whitened}}$) of SO_2, we can unambiguously interpret whether the observed spectral anomalies are explicitly caused by the target gas, thereby effectively eliminating false positive detections. In our retrieval process, only the observations initially flagged with an HRI greater than 3 are subject to this spectral whitening transformation. Furthermore, the correlation coefficient between the whitened spectrum and the whitened Jacobian is calculated, and any detections with a correlation coefficient of less than 0.22 are completely filtered out to ensure high confidence in the SO_2 signals.

https://doi.org/10.5194/egusphere-2026-5017
Preprint. Discussion started: 22 September 2026

Data availability

The SO_2 retrieval results from FengYun and CrIS in this study will be uploaded to a permanent repository upon publication. The FY-3E/HIRAS-II Level 1 data are publicly available from the FengYun Satellite Data Center (https://data.nsmc.org.cn/DataPortal/en/home/index.html). The JPSS-2/CrIS Level 1B data are available at GES DISC (https://search.earthdata.nasa.gov/). The IASI Level 2 SO_2 data are available from the IASI Portal (https://iasi.aeris-data.fr/) with datasets accessible via https://dx.doi.org/10.25326/869 for Metop-B and https://dx.doi.org/10.25326/868 for Metop-C. The TROPOMI SO_2 and NO_2 data can be downloaded via the Copernicus Data Space Ecosystem (https://browser.dataspace.copernicus.eu/). The HYSPLIT model is publicly available from the NOAA Air Resources Laboratory (https://www.ready.noaa.gov/HYSPLIT.php). The EDGAR v8.1 emission inventory is available from the European Commission Joint Research Centre (https://edgar.jrc.ec.europa.eu/dataset_ap80). The MODIS Fire Radiative Power products (MOD14 and MYD14) are available from the NASA Land Processes Distributed Active Archive Center (https://lpdaac.usgs.gov/product_search/). The CAMS SO_2 data are available from ECMWF (https://www.ecmwf.int/en/forecasts/dataset/cams-global-atmospheric-composition-forecasts).

Author contributions

Shangyi Liu: Methodology, Software, Validation, Formal analysis, Writing– original draft, Writing– review & editing. **Cathy Clerbaux:** Resources, data curation, Writing- Reviewing and Editing. **Anne Boynard**: Writing-review and Editing. **Mingjian Gu:** Resources, data curation, Writing- Reviewing and Editing. **Chengli Qi:** Resources, data curation, Writing- Reviewing and Editing. **Bruno Franco:** Resources, data curation, Writing- Reviewing and Editing. **Lieven Clarisse:** Resources, data curation, Writing- Reviewing and Editing. **Shan Han:** Writing– review & editing. **Mengya Sheng:** Writing– review & editing. **Nicolas Theys:** Resources, data curation, Writing- Reviewing and Editing. **Zhao-Cheng Zeng:** Conceptualization, Methodology, Software, Supervision, Writing– review & editing, Funding acquisition

Competing interests

The contact author has declared that none of the authors has any competing interests.

Acknowledgements

S. Liu acknowledges the financial support from the China Scholarship Council (CSC). The research has been supported by the HIRS Prodex arrangement (ESA-BELSPO). L. Clarisse is Senior Research Associate supported by the Belgian F.R.S.-FNRS. N. Theys acknowledges financial support from ESA S5P PAL, ESA S5P ATM-MPC and Belgium Prodex TRACE-S5P projects. This study was supported by the High-Performance Computing Platform of Peking University.

https://doi.org/10.5194/egusphere-2026-5017
Preprint. Discussion started: 22 September 2026

Financial support

This study was supported by the National Natural Science Foundation of China (No. 42275142) and the National Key R&D Program of China (No. 2022YFA1003800).

References

Al Jazeera. Israeli attacks on Iran fuel sites aim 'to break resilience of people'. Al Jazeera, 9 March 2026. https://www.aljazeera.com/features/2026/3/9/israeli-attacks-on-iran-fuel-sites-aim-to-break-resilience-of-people.

Atmospheric and Environmental Research. Line-by-line radiative transfer model (LBLRTM). Atmos. Environ. Res. 2025. Retrieved from https://github.com/AERRC/LBLRTM.

Bakan, S.; et al. Climate response to smoke from the burning oil wells in Kuwait. Nature. 1991, 351 (6325), 367–371.

Bauduin, S.; Clarisse, L.; Hadji-Lazaro, J.; Theys, N.; Clerbaux, C.; Coheur, P.-F. Retrieval of near-surface sulfur dioxide (SO2) concentrations at a global scale using IASI satellite observations. Atmos. Meas. Tech. 2016, 9 (2), 721–740.

BBC. Air strikes cause black rain and "unprecedented" pollution in Tehran, scientists say. BBC News, 10 March 2026. https://www.bbc.com/news/articles/cqxd1nv3re2o.

Beirle, S.; Borger, C.; Dörner, S.; Eskes, H.; Kumar, V.; de Laat, A.; Wagner, T. Catalog of NOx emissions from point sources as derived from the divergence of the NO2 flux for TROPOMI. Earth Syst. Sci. Data. 2021, 13, 2995–3012.

Björnham, O.; Grahn, H.; von Schoenberg, P.; Liljedahl, B.; Waleij, A.; Brännström, N. The 2016 Al-Mishraq sulphur plant fire: Source and health risk area estimation. Atmos. Environ. 2017, 169, 287–296.

Carboni, E.; Grainger, R.; Walker, J.; Dudhia, A.; Siddans, R. A new scheme for sulphur dioxide retrieval from IASI measurements: Application to the Eyjafjallajökull eruption of April and May 2010. Atmos. Chem. Phys. 2012, 12, 11417–11434.

Carn, S. A.; Clarisse, L.; Prata, A. J. Multi-decadal satellite measurements of global volcanic degassing. J. Volcanol. Geophys. Res. 2016, 311, 99–134.

CEOBS. Black rain: the health and environmental risks from Tehran's oil fires. Conflict and Environment Observatory, 9 March 2026. https://ceobs.org/black-rain-the-health-and-environmental-risks-from-tehrans-oil-fires/.

Clarisse, L.; Fromm, M.; Ngadi, Y.; Emmons, L.; Clerbaux, C.; Hurtmans, D.; Coheur, P.-F. Intercontinental transport of anthropogenic sulfur dioxide and other pollutants: An infrared remote sensing case study. Geophys. Res. Lett. 2011, 38 (19), L19806.

Clarisse, L.; Coheur, P.-F.; Prata, F.; Hadji-Lazaro, J.; Hurtmans, D.; Clerbaux, C. A unified approach to infrared aerosol remote sensing and type specification. Atmos. Chem. Phys. 2013, 13 (4), 2195–2221.

Clarisse, L.; Coheur, P.-F.; Theys, N.; Hurtmans, D.; Clerbaux, C. The 2011 Nabro eruption, a SO2 plume height analysis using IASI measurements. Atmos. Chem. Phys. 2014, 14, 3095–3111.

https://doi.org/10.5194/egusphere-2026-5017
Preprint. Discussion started: 22 September 2026

Clarisse, L.; Franco, B.; Fabris, L.; Theys, N.; Hadji-Lazaro, J.; Hurtmans, D.; Clerbaux, C.; Coheur, P. An 18-year record of atmospheric sulphur dioxide (SO2) derived from IASI measurements. Earth Syst. Sci. Data Discuss. [preprint], 2026, in review. https://doi.org/10.5194/essd-2026-186.

Crippa, M.; Guizzardi, D.; Pagani, F.; Schiavina, M.; Melchiorri, M.; Pisoni, E.; Graziosi, F.; Muntean, M.; Maes, J.; Dijkstra, L.; Van Damme, M.; Clarisse, L.; Coheur, P. Insights into the spatial distribution of global, national, and subnational greenhouse gas emissions in the Emissions Database for Global Atmospheric Research (EDGAR v8.0). Earth Syst. Sci. Data. 2024, 16, 2811–2830.

De Longueville, H.; Clarisse, L.; Whitburn, S.; Franco, B.; Bauduin, S.; Clerbaux, C.; et al. Identification of short and long-lived atmospheric trace gases from IASI space observations. Geophys. Res. Lett. 2021, 48 (5).

Fioletov, V.; McLinden, C. A.; Griffin, D.; Theys, N.; Loyola, D. G.; Hedelt, P.; Krotkov, N. A.; Li, C. Anthropogenic and volcanic point source SO2 emissions derived from TROPOMI on board Sentinel-5 Precursor: first results. Atmos. Chem. Phys. 2020, 20, 5591–5607.

Flemming, J.; Huijnen, V.; Arteta, J.; Bechtold, P.; Beljaars, A.; Blechschmidt, A.-M.; Diamantakis, M.; Engelen, R. J.; Gaudel, A.; Inness, A.; Jones, L.; Josse, B.; Katragkou, E.; Marecal, V.; Peuch, V.-H.; Richter, A.; Schultz, M. G.; Stein, O.; Tsikerdekis, A. Tropospheric chemistry in the Integrated Forecasting System of ECMWF. Geosci. Model Dev. 2015, 8, 975–1003.

Fromm, M.; Lindsey, D. T.; Servranckx, R.; Yue, G.; Trickl, T.; Sica, R.; Doucet, P.; Godin-Beekmann, S. The untold story of pyrocumulonimbus. Bull. Amer. Meteorol. Soc. 2010, 91 (9), 1193–1209.

Giglio, L.; Schroeder, W.; Justice, C. O. The Collection 6 MODIS active fire detection algorithm and fire products. Remote Sens. Environ. 2016, 178, 31–41.

Hersbach, H.; Bell, B.; Berrisford, P.; Hirahara, S.; Horányi, A.; Muñoz-Sabater, J.; Nicolas, J.; Peubey, C.; Radu, R.; Schepers, D.; Simmons, A.; Soci, C.; Abdalla, S.; Abellan, X.; Balsamo, G.; Bechtold, P.; Biavati, G.; Bidlot, J.; Bonavita, M.; et al. The ERA5 global reanalysis. Q. J. R. Meteorol. Soc. 2020, 146 (730), 1999–2049.

Hobbs, P. V.; Radke, L. F. Airborne studies of the smoke from the Kuwait oil fires. Science 1992, 256 (5059), 987–991.

Hyman, D. M.; Pavolonis, M. J. Probabilistic retrieval of volcanic SO2 layer height and partial column density using the Cross-track Infrared Sounder (CrIS). Atmos. Meas. Tech. 2020, 13 (11), 5891–5921.

Inness, A.; Ades, M.; Agustí-Panareda, A.; Barré, J.; Benedictow, A.; Blechschmidt, A.-M.; Dominguez, J. J.; Engelen, R.; Eskes, H.; Flemming, J.; Huijnen, V.; Jones, L.; Kipling, Z.; Massart, S.; Parrington, M.; Peuch, V.-H.; Razinger, M.; Remy, S.; Schulz, M.; Suttie, M. The CAMS reanalysis of atmospheric composition. Atmos. Chem. Phys. 2019, 19, 3515–3556.

Khaleej Times. WHO warns of ‘black rain’ health risks after Israeli strikes on Iran oil facilities. Khaleej Times, 11 Mar 2026. https://www.khaleejtimes.com

Krotkov, N. A.; Carn, S. A.; Krueger, A. J.; Bhartia, P. K.; Yang, K. Band residual difference algorithm for retrieval of SO2 from the Aura Ozone Monitoring Instrument (OMI). IEEE Trans. Geosci. Remote Sens. 2006, 44 (5), 1259–1266.

https://doi.org/10.5194/egusphere-2026-5017
Preprint. Discussion started: 22 September 2026

Lawrence, M. J.; et al. The effects of modern war and military activities on biodiversity and the environment. Environ. Rev. 2015, 23 (4), 443–460.

Liu, S.; Zheng, Y.; Sheng, M.; Lee, L.; Qi, C.; Lu, F.; Franco, B.; Clarisse, L.; Clerbaux, C.; Theys, N.; Kim, J.; Zeng, Z.-C. High-frequency monitoring of SO2 plumes from moderate-scale volcanic eruptions using a synergy of GEO and LEO satellites: A case study of the 2024 Kanlaon eruption. EGUsphere [preprint], 2026. https://doi.org/10.5194/egusphere-2026-1745.

Long, B.; Bao, J. L.; Truhlar, D. G. Reaction of SO2 with OH in the atmosphere. Phys. Chem. Chem. Phys. 2017, 19 (11), 8091–8100.

Manolakis, D. G.; Lockwood, R. B.; Cooley, T. W. Hyperspectral Imaging Remote Sensing: Physics, Sensors, and Algorithms; Cambridge University Press: Cambridge, UK, 2016.

Mao, Y.; Ju, W.; Wang, H.; Liu, L.; Wang, H.; Feng, S.; Jia, M.; Jiang, F. Inversion-based assessment of anthropogenic NOx emission changes in Ukraine during the 2022–2023 war using TROPOMI satellite data. Atmos. Chem. Phys. 2025, 25, 14187–14209.

Masuda, K.; Takashima, T.; Takayama, Y. Emissivity of pure and sea waters for the model sea surface in the infrared window regions. Remote Sens. Environ. 1998, 24, 313–329.

Rawtani, D.; et al. Environmental damages due to war in Ukraine: A perspective. Sci. Total Environ. 2022, 850, 157932.

Rodgers, C. D. Inverse Methods for Atmospheric Sounding: Theory and Practice; World Scientific: Singapore, 2000.

Seemann, S. W.; Borbas, E. E.; Knuteson, R. O.; Stephenson, G. R.; Huang, H.-L. Development of a global infrared land surface emissivity database for application to clear sky sounding retrievals from multispectral satellite radiance measurements. J. Appl. Meteorol. Climatol. 2008, 47 (1), 108–123.

Solomon, S.; et al. On the stratospheric chemistry of midlatitude wildfire smoke. Proc. Natl. Acad. Sci. U.S.A. 2022, 119 (10), e2117325119.

Stein, A. F.; Draxler, R. R.; Rolph, G. D.; Stunder, B. J. B.; Cohen, M. D.; Ngan, F. NOAA's HYSPLIT atmospheric transport and dispersion modeling system. Bull. Amer. Meteorol. Soc. 2015, 96 (12), 2059–2077.

Theys, N.; De Smedt, I.; Yu, H.; Danckaert, T.; van Gent, J.; Hörmann, C.; Wagner, T.; Hedelt, P.; Bauer, H.; Romahn, F.; Pedergnana, M.; Loyola, D.; Van Roozendael, M. Sulfur dioxide retrievals from TROPOMI onboard Sentinel-5 Precursor: Algorithm theoretical basis. Atmos. Meas. Tech. 2017, 10, 119–153.

van Geffen, J.; Eskes, H.; Compernolle, S.; Pinardi, G.; Verhoelst, T.; Lambert, J.-C.; Sneep, M.; ter Linden, M.; Ludewig, A.; Boersma, K. F.; Veefkind, J. P. Sentinel-5P TROPOMI NO_2 retrieval: Impact of version v2.2 improvements and comparisons with OMI and ground-based data. Atmos. Meas. Tech. 2022, 15 (7), 2037–2060.

Walker, J. C.; Dudhia, A.; Carboni, E. An effective method for the detection of trace species demonstrated using the MetOp Infrared Atmospheric Sounding Interferometer. Atmos. Meas. Tech. 2011, 4, 1567–1580.

Yang, K., Dickerson, R. R., Carn, S. A., Ge, C., and Wang, J.: First observations of SO2 from the satellite Suomi NPP OMPS: Widespread air pollution events over China. Geophys. Res. Lett. 2013, 40 (18), 4957–4962.

https://doi.org/10.5194/egusphere-2026-5017
Preprint. Discussion started: 22 September 2026

Yin, Z., Chen, Y., Bu, Z. et al. Analysis of SO2 Emissions and Dispersion from the Fire at the Oil Storage and Refining Plant in Tehran, Iran, in March 2026. Adv. Atmos. Sci. 2026.

Yu, P.; Toon, O. B.; Bardeen, C. G.; et al. Black carbon lofts wildfire smoke high into the stratosphere to form a persistent aerosol record. *Science.* 2019, *365* (6453), 587–590.

Zeng, Z.-C. Global carbon monoxide retrieval from the hyperspectral infrared atmospheric sounder-II onboard FengYun-3E in a dawn-dusk sun-synchronous orbit. J. Quant. Spectrosc. Radiat. Transfer. 2025, 109336.

Zeng, Z.-C.; Lee, L.; Qi, C. Diurnal carbon monoxide observed from a geostationary infrared hyperspectral sounder: First result from GIIRS on board FengYun-4B. Atmos. Meas. Tech. 2023, 16 (12), 3059–3083.

Zeng, Z.-C.; Clarisse, L.; Franco, B.; Clerbaux, C.; Theys, N.; Qi, C.; Lee, L.; Zhu, L.; Hu, X.; Gu, M.; Zhang, P. Volcanic sulfur dioxide monitored from a constellation of FengYun hyperspectral infrared sounders in dawn-dusk, mid-morning, and afternoon sun-synchronous orbits. Remote Sens. Environ. 2025, 331, 115057.